Powder Technology 413 (2023) 118035

Contents lists available at ScienceDirect

Powder Technology

journal homepage: www.journals.elsevier.com/powder-technology

A methodology for tribocharger design optimisation using the Discrete Element Method (DEM)

J.N. Rasera [a,b,*], J.J. Cilliers [a], J.-A. Lamamy [b], K. Hadler [a,c]

[a] Imperial College London, Department Earth Sciences and Engineering, Exhibition Road, London, SW7 2AZ, United Kingdom
[b] ispace Europe S.A., 5, rue de l'Industrie, L-1811 Luxembourg
[c] European Space Resources Innovation Centre, 41, rue du Brill, L- 4422 Sanem, Luxembourg

HIGHLIGHTS

- Computational approaches provide scope to investigate design optimisation problems.
- The DEM is applied in a novel manner to optimise the design of a tribocharging device.
- A 3D DEM model is used to predict the performance of an optimal design.
- An approach to predict tribocharger performance from limited inputs is provided.

GRAPHICAL ABSTRACT

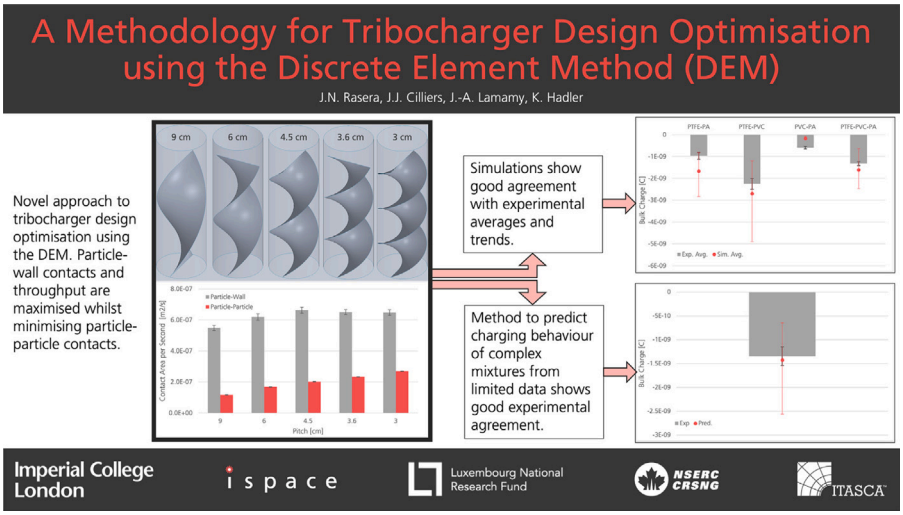

ARTICLE INFO

Keywords:
Tribocharger design
Discrete Element Method (DEM)
Design optimisation
Computational electrostatics

ABSTRACT

Tribocharger design optimisations presented in the literature are based typically on experimental investigations. While this approach is useful and necessary to evaluate the performance of a design, experimental investigations are limited to studying a finite matrix of parameters. Computational approaches, such as the discrete element method (DEM), offer greater flexibility, however they have not been used previously for tribocharger design optimisation. This work presents a novel approach using the DEM to study the effect of different tribocharger designs on the charging process using particle–wall and particle–particle contact areas as proxies for charge transfer. The bulk sample charge output from the model are compared with bulk charges measured experimentally, showing good agreement. Furthermore, a method to predict approximately the charging behaviour of complex mixtures from linear combinations of the simulation outputs of single species, single size particle samples is presented, demonstrating good agreement.

* Corresponding author at: Imperial College London, Department Earth Sciences and Engineering, Exhibition Road, London, SW7 2AZ, United Kingdom.
E-mail address: j.rasera@imperial.ac.uk (J.N. Rasera).

https://doi.org/10.1016/j.powtec.2022.118035
Received 12 August 2022; Received in revised form 12 October 2022; Accepted 17 October 2022
Available online 26 October 2022

Nomenclature

Constants

ϵ_0	Permittivity of free space F/m
$\vec{g}$	Acceleration due to gravity m/s^2
e	Electron charge magnitude C

Subscripts & Superscripts

$*$	Effective value, evaluated from two interacting particles
0	Indicates value at beginning of timestep
d	Dashpot
h	Hertz
i	Particle i
j	Particle j
n	Normal component
s	Shear component
sat	Saturation

Variables

β	Damping coefficient
ΔA	Change in contact area m^2
Δq	Change in charge C
δ_c	Contact gap m
δ_e	Charge transfer cutoff distance m
Γ	Charge transfer limitation parameter V/m
$\hat{n}$	Unit normal vector
$\hat{r}$	Radial unit vector
κ_c	Charging efficiency
μ	Coefficient of friction
ν	Poisson's ratio
Φ	Surface potential difference V
ϕ	Effective work function eV
ρ	Density kg/m^3
σ	Surface charge density C/m^2
σ_f	Saturation charge density of an infinite plane C/m^2
$\vec{a}$	Translational acceleration m/s^2
$\vec{E}$	Electric field strength V/m
$\vec{F}_c$	Local contact force N
$\vec{F}_d$	Dashpot force N
$\vec{F}_h$	Non-linear Hertz force N
$\vec{M}_c$	Moment at the point of contact Nm
$\vec{v}_{ij}$	Relative velocity m/s
$\vec{x}$	Position m
A	Area m^2
G	Shear modulus Pa
m	Mass kg
n	Number of particles within the domain
q	Charge C
r	Radius m
r_{cutoff}	Strong interaction cutoff radius m
t	Time s
Y	Young's modulus Pa

1. Introduction

Tribocharging, or triboelectrification, is a method of imparting electrostatic charge on an object by frictional contact. This phenomenon has been known and observed for millennia [1], however the physical mechanisms that drive it are not well understood [2–4]. The magnitude of charge sustained on a particle's surface, as well as the quantity of charge transferred during a contact event, depend on factors such as humidity, temperature, impact velocity, flow density, and material composition [5–7].

The tribocharging of particulate materials through conveyance processes is often undesirable, and many studies look to minimise its impact (e.g., [8–11]). However, the same effect can be exploited for processes such as material separation in recycling (e.g., [12–20]), printer toner application (e.g., [21–26]), and dry mineral beneficiation (e.g., [5,27–37]).

For separation applications, it is necessary to optimise the design of the tribocharger to maximise the charge transferred to each particle. There are two main approaches to optimise such a process: experimentally and computationally.

Several studies have studied experimentally the choice of tribocharger material (e.g., [38–43]). Others have looked into the impact of the geometry of the charger itself (e.g., [35,36,41–45]). While all of these studies have provided valuable data and insight for the optimisation of a tribocharger design, they are limited ultimately in the number of materials and designs that can realistically be tested.

Substantial effort has been put towards developing and evaluating means to model the charge transfer process [1,46–60]. However, the use of numerical methods, particularly using the discrete element method (DEM), to optimise the design of a tribocharger has not been investigated.

Cundall and Strack's [61,62] discrete element method is of particular interest for modelling triboelectrification [46,50–58]. The DEM lends itself to coupling with tribocharging models, as parameters necessary for evaluating charge transfer are extracted easily. A number of tribocharging models that have been presented previously in the literature that show good agreement with experimental data [50–55,58,63]. These models, however, are typically dependent on poorly defined quantities, such as surface work function for insulating materials [46]. Rasera et al. [46] presented a straightforward, empirical approach to determine tribocharging model parameters that de-emphasises the importance of these poorly defined parameters. This method requires limited input data to successfully extrapolate key model parameters for different particle sizes. However, their work was limited to basic geometries, and did not consider mixtures of particles of different species or sizes.

The aims of this work are threefold: to present and demonstrate a DEM-based tribocharger design optimisation method; to extend the work of Rasera et al. [46] by simulating the charging behaviour of ideal particles using an optimised charger design and to compare it to experimental data; and to evaluate what, if any, predictions can be made about the charging behaviour of complex, heterogeneous samples from the model outputs of homogeneous samples.

This article is divided into five sections. Following the introduction, Section 2 provides an overview of the mathematical models employed. Section 3 outlines the experimental methods used to determine the DEM model parameters, as well as to measure the charging performance of the optimised charger design. Section 4 presents the optimised charger design, as well as an evaluation of the performance of Rasera et al.'s [46] charging model against the experimental results. Finally, Section 5 summarises the main conclusions from this work.

2. Mathematical models

The modelling presented in this work is an extension of that published previously by Rasera et al. [46]; the reader is encouraged to consult that publication for further detail. A brief overview of the approach is presented here for completeness. Itasca Consulting Group's Particle Flow Code (PFC) is the DEM solver used in this work.

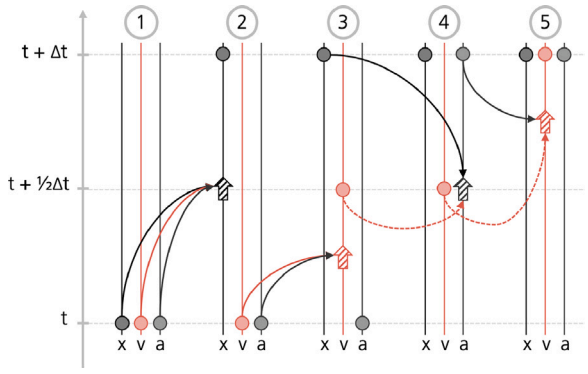

Fig. 1. Overview of the second order Velocity Verlet algorithm, from Rasera et al. [46], adapted from Holm [65]. 1. Initial position. 2. Determine new particle position by $\vec{x}(t+\Delta t) = \vec{x}(t)+\vec{v}(t)\Delta t+0.5\vec{a}(t)\Delta t^2$. 3. Find velocity at $t+\Delta t/2$ by $\vec{v}(t+0.5\Delta t) = \vec{v}(t)+0.5\vec{a}(t)\Delta t$. 4. Determine the acceleration from the body forces using Newton's Law. 5. Calculate the final velocity by $\vec{v}(t+\Delta t) = \vec{v}(t+0.5\Delta t) + 0.5\vec{a}(t+0.5\Delta t)\Delta t$.

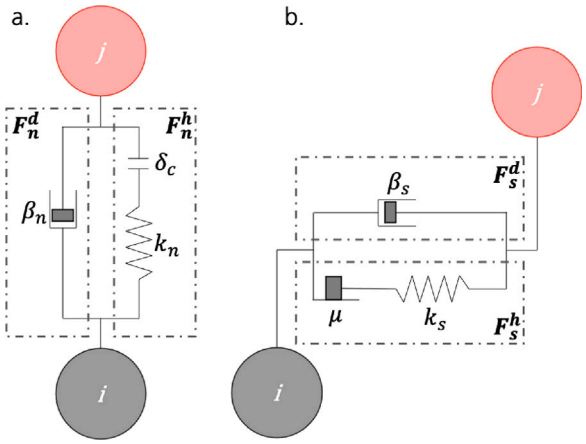

Fig. 2. Cartoon overview of the force models for the normal (a) and the shear (b) components. From Rasera et al. [46], adapted from Laurentie et al. and Itasca CG [50,51,64].

2.1. Mechanical

Cundall and Strack [61] developed the DEM to simulate and analyse rock mechanics and impacts. Particle interactions are treated as dynamic processes. Contact forces and relative displacements are evaluated by tracking the motion of individual particles. Over each timestep, particle accelerations and velocities are kept constant. Discrete element models employ Newton's second law of motion and a force–displacement relationship to evaluate particle interactions, forces and motion. Integrating Newton's law once provides relative particle motion characteristics, and integrating a second time solves for particle positions. The force–displacement method selected determines the way that contact forces are evaluated and applied to each contact [64].

The equations of translational motion are solved using a second-order Velocity Verlet algorithm (Fig. 1).

The Hertz–Mindlin force–displacement model is employed (following [50–56,66,67]) as it considers both normal and shear force components. In this model, particle stiffness is assumed to be non-linear. All interactions are assumed to be elastic; plastic deformation is not considered.

The Hertz–Mindlin contact model is applied to all interactions. The contact force, $\vec{F}_c$ is evaluated by:

$$\vec{F}_c = \vec{F}_h + \vec{F}_d \tag{1}$$

where $\vec{F}_h$ is the nonlinear Hertz force and $\vec{F}_d$ is the dashpot force (Fig. 2). The contact interface of the Hertz–Mindlin model allows for rotational motion of particles, hence the moment at the point of contact is zero ($\vec{M}_c \equiv 0$).

The details of the solver algorithm used by PFC is presented by Itasca [64]. In summary, the method is as follows:

1. Evaluate and update the Hertz normal force:

$$F_n^h = \begin{cases} \frac{4}{3} Y^* \sqrt{r^*} \delta_c^{3/2}, & \text{if } \delta_c \le 0.0 \\ 0.0, & \text{otherwise} \end{cases} \tag{2}$$

where δ_c is the contact gap extracted from the relative particle positions (negative if contact is active). The effective contact radius, r^*, and the effective modulus of elasticity, Y^*, are found by:

$$r^* = \begin{cases} \frac{r_i r_j}{r_i + r_j}, & \text{if particle–particle,} \\ r_i, & \text{if particle–wall,} \end{cases} \tag{3}$$

and,

$$Y^* = \left(\frac{1-\nu_i}{2G_i} + \frac{1-\nu_j}{2G_j} \right)^{-1}, \tag{4}$$

respectively. Here, ν is Poisson's ratio and G is the shear modulus. The subscripts i and j denote the ith and jth particles, respectively, in the system. In particle–wall interactions, j refers to the wall.

2. Update the Hertz shear force:

$$\vec{F}_s^h = \begin{cases} \vec{F}_s^*, & \text{if } ||\vec{F}_s^*|| \le \mu F_n^h, \\ \mu F_n^h \frac{\vec{F}_s^*}{||\vec{F}_s^*||}, & \text{otherwise,} \end{cases} \tag{5}$$

where μ is the minimum coefficient of friction between the two particles, and $\vec{F}_s^*$ is the initial estimate of the shear force [64], given by:

$$\vec{F}_s^* = (\vec{F}_s^h)_0 - 8G^* \sqrt{r^* \delta_c}. \tag{6}$$

Here, $(\vec{F}_s^h)_0$ is the shear force at the start of the timestep . If the magnitude of the Hertz shear is equal to the friction force, μF_n^h, then it is assumed that the contact is slipping.

3. Update the dashpot normal force:

$$F_n^d = 2\sqrt{\frac{5}{6}} \beta \sqrt{2m^* Y^* \sqrt{r^* \delta_c}} \vec{v}_{ij}^n, \tag{7}$$

where β is the damping ratio, $\vec{v}_{ij}^n$ is the relative velocity in the normal direction, and m^* is the effective contact mass, given by:

$$m^* = \begin{cases} \frac{m_i m_j}{m_i + m_j}, & \text{if particle–particle,} \\ m_i, & \text{if particle–wall.} \end{cases} \tag{8}$$

4. Update the dashpot shear force:

$$\vec{F}_s^d = \begin{cases} 2\sqrt{\frac{5}{6}} \beta \sqrt{8m^* G^* \sqrt{r^* \delta_c}} \vec{v}_{ij}^s, & \text{if slipping,} \\ 0, & \text{otherwise,} \end{cases} \tag{9}$$

where $\vec{v}_{ij}^s$ is the relative velocity in the shear direction, and G^* is the effective shear modulus, given by:

$$G^* = \left(\frac{2-\nu_i}{G_i} + \frac{2-\nu_j}{G_j} \right)^{-1} \tag{10}$$

2.2. Tribocharging

The tribocharging model employed uses the high-density limit of surface state theory to describe the charge transferred between two surfaces, following Schein et al. [63], Matsusaka et al. [68], Laurentie et al. [50,51], and Kolehmainen et al. [52–54]. This is given by:

$$\sigma = \kappa_c \varepsilon_0 \left(\frac{\phi_i - \phi_j}{\delta_e e} - \vec{E}_{contact} \cdot \hat{n}_{ij} \right) \tag{11}$$

Here, σ is the charge transferred per unit area; κ_c is the empirically-derived charging efficiency; ε_0 is the permittivity of free space; δ_e is the separation distance between two particles at which point charge transfer ceases; e is the magnitude of the electron charge; ϕ_i and ϕ_j are the effective work functions; $\vec{E}_{contact}$ is the electrostatic field at the point of contact; and, $\hat{n}_{ij}$ is the unit normal vector pointing from particle i to j at the point of contact. Following Rasera et al. [46], the $(\phi_i - \phi_j)/(\delta_e e)$ term is replaced by the charge transfer limitation parameter, Γ. The expression is then rearranged in terms of the quantity of charge transferred, Δq, a function of the change in contact area during a collision, ΔA:

$$\Delta q = \Delta A \kappa_c \varepsilon_0 \left(\Gamma - \vec{E}_{contact} \cdot \hat{n}_{ij} \right). \tag{12}$$

This form of the equation becomes more suitable for implementation in the DEM. The contact area between two objects is approximated by $A = \pi r^* \delta_c$ [50,51].

For particle–wall interactions, Γ is found to be (following [46]):

$$\Gamma = \frac{q_{i,sat}}{4\pi\varepsilon_0 r_i^2} = \frac{\sigma_{i,sat}}{\varepsilon_0}, \tag{13}$$

where q_{sat} is the experimentally derived saturation charge of a particle, r is the particle radius, and $\sigma_{i,sat}$ is the surface charge density at saturation. For particle–particle interactions [46]:

$$\Gamma = \frac{\sigma_{i,sat} - \sigma_{j,sat}}{\varepsilon_0}. \tag{14}$$

For particle–particle contacts, Γ tends to zero when the particles are the same size and material. The charge transfer limitation parameter is dependent on electrostatic parameters and particle size only, and is independent of particle kinematics and contact area.

The value of $\sigma_{i,sat}$ for a different particle size of a particular material can be determined semi-empirically from saturation data of other size classes using the model of Cruise et al. [7]:

$$\sigma_{i,sat} = \frac{\sigma_f}{\varepsilon_0} + \frac{\Phi_{sat}}{r_i}, \tag{15}$$

where σ_f is the saturation charge density of an infinite plane, and Φ_{sat} is the surface potential difference at saturation; both σ_f and Φ_{sat} are assumed to be constant across all particle sizes. This model is used to predict the saturation surface charge density of particles of different sizes.

The charging efficiency term, κ_c, must be evaluated empirically. The calculation of κ_c is dependent on the interaction type (particle–particle or particle–wall), as well as the particle size and contact area. Previous studies have largely ignored κ_c, assuming it to be 1 [46]. However, Rasera et al. [46] found that this term plays an important role in the modelling of the tribocharging process. It should be noted that 'efficiency' is a misnomer in this case, however as the terminology has been established previously, it is maintained herein.

For particle–wall contacts, κ_c is given by:

$$\kappa_c = \frac{4\pi r^2 \Delta q}{\Delta A (q_{i,sat} - q_i)}, \tag{16}$$

where q_{sat} is the saturation charge, and q is the actual charge on that particle's surface [46].

For dissimilar particle–particle contacts, κ_c is given by [46]:

$$\kappa_c = \frac{4\pi r_i^2 r_j^2 \Delta q}{\Delta A [r_j^2 (q_{i,sat} - q_i) - r_i^2 (q_{j,sat} - q_j)]}, \tag{17}$$

whereas for similar particles, by [46]:

$$\kappa_c = \frac{4\pi r^2 \Delta q}{\Delta A (q_j - q_i)}. \tag{18}$$

When two similar particles are neutralised prior to experimentation, κ_c may be approximated by [46]:

$$\kappa_c = \frac{4\pi r^2}{\Delta A}. \tag{19}$$

The value of ΔA is dependent on the mechanical properties of the particle as well as the relative impact velocity of the particle. In this work, the value of ΔA is determined by simulating the single-contact interactions with the DEM.

As Γ and κ_c are based on empirically-derived properties and data, both have maxima, minima, and average values. The maxima and minima are evaluated using the upper and lower bounds of 95% confidence intervals of the particle radii, initial charge, charge transfer, and contact area from experimental data.

2.3. Electrostatic fields

Electrostatic fields obey the law of superposition. The electrostatic field contributions can be broken down into several types, such that:

$$\vec{E}_{contact} = \vec{E}_{ij} + \vec{E}_{near} \tag{20}$$

Here, $\vec{E}_{ij}$ is the field due to the charges carried by particles i and j in the case of particle–particle contact, or by particle i alone in a particle–wall interaction. $\vec{E}_{ij}$ is given by Coulomb's Law:

$$\vec{E}_{ij} = \begin{cases} \left(\frac{q_j}{4\pi\varepsilon_0 r_j^2} - \frac{q_i}{4\pi\varepsilon_0 r_i^2} \right) \hat{r}, & \text{if particle–particle,} \\ \frac{-q_i}{4\pi\varepsilon_0 r_i^2} \hat{r}, & \text{if particle–wall,} \end{cases} \tag{21}$$

where $\hat{r}$ is the radial unit vector pointing between particle centroids.

The near field contributions, $\vec{E}_{near}$, results from the charge on nearby particles and particle image charges using a modified version of the direct truncation (DT) method presented elsewhere [52–54,56,57,69]. The DT method uses pairwise sums to determine the field contributions from particles that fall within a user-defined cutoff radius, r_{cutoff}, as follows:

$$\vec{E}_{near,i} = \frac{1}{4\pi\varepsilon_0} \sum_{k=1,k\neq i,||\vec{x}_i - \vec{x}_k|| \leq r_{cutoff}}^{n} q_k \frac{\vec{x}_i - \vec{x}_k}{||\vec{x}_i - \vec{x}_k||^3}, \tag{22}$$

where $\vec{x}$ is the position vector of each particle.

However, because the tribocharger is assumed to be made of aluminium and to be grounded, and since all of the designs considered use grounded baffles, the number jth particles 'seen' by any given particle i is restricted by the charger's internal geometry. Hence, the modified DT (mDT) incorporates an additional check to ensure that two particles are not separated by a grounded surface (see Fig. 3). The mDT method is attractive because it offers good accuracy without compromising greatly on computational performance.

Here, r_{cutoff} is defined as 1/4 the overall length of the tribocharger baffle. Due to the screening effect caused by the grounded aluminium baffle running through the domain, the cutoff distance was chosen to maximise the volume 'seen' by a particle whilst transiting the domain. Because the number of particles in the domain is restricted, this choice of r_{cutoff} maximised the number of particles contributing to the pairwise sum calculation whilst maintaining reasonable computation times.

The algorithm for modelling triboelectric charging is as follows:

1. Update the particle positions and velocities using the laws of motion.
2. Identify contacting bodies (particles and/or walls).
3. Determine the overlap and evaluate the change in contact area.

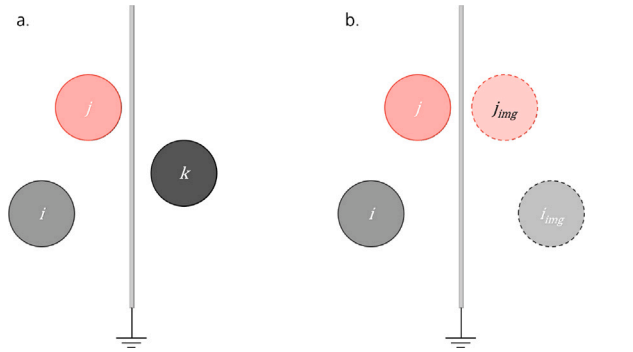

Fig. 3. A representative example of the mDT method. In (a), both particles j and k are within the cutoff distance of i. Particle k, however, is separated from i by a grounded, conducting plane. As such, the electrostatic field contributions 'felt' by i are due to the charge of j, as well as the image charges of both i and j due to the grounded plane (b).

4. Find the electrostatic field at the centroid of each particle. If the contact is between two particles, use linear interpolation to find the field at the point of contact. If the contact is between a particle and a wall, calculate the field at the point of contact directly using Eq. (21).
5. Evaluate the quantity of charge exchanged.
6. Determine the electrostatic force acting on each particle.
7. Use the Hertz model to update the mechanical forces and moments.

3. Tribocharger design optimisation

3.1. Baseline design

A tribocharger design employed with success in the literature is described by Trigwell et al. [42,43] and Quinn et al. [70]. In these works, the authors looked to enrich the mineral ilmenite using a static tribocharger and free-fall electrostatic separator. Their design consisted of an aluminium tube with a series of twisted aluminium baffles suspended inside, as shown in Fig. 4. The particles employed in this study are appreciably larger than the fine powders used in those studies. To ensure that the charger would not become blocked both during simulation and experimentation, the dimensions reported in Trigwell et al. and Quinn et al. were scaled up. The height of the baffle was chosen to be 4.5 cm and the inner diameter of the charger tube to be 1.9 cm. These dimensions are taken as the baseline design geometry.

Furthermore, to minimise the computational cost of each simulation, a single baffle is modelled. It is assumed that the optimal design would hold were a longer insert used.

3.2. Parameter of interest

From the findings of Rasera et al. [46] and Cruise et al. [7], two primary design criteria are identified:

1 Particle–wall contacts must be maximised to ensure the most predictable transfer of charge, as particle–particle interactions are inherently stochastic; and,
2 The number of particles within a given charging volume must be kept to a minimum as the bulk saturation charge and charge transfer are found to be suppressed in the presence of increasing numbers of particles.

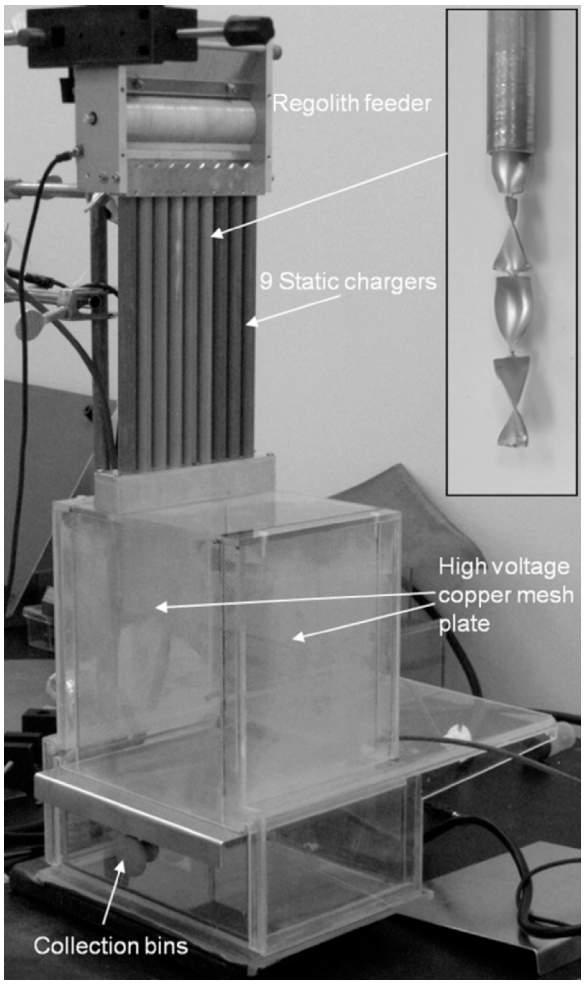

Fig. 4. The free fall triboelectric separator employed by Trigwell et al. [42,43] and Quinn et al. [70].

Both criteria are functions of the tribocharger geometry and inlet flow velocity. However, the inlet velocities are independent of the charger geometry. Therefore, in this study, the internal geometry of the tribocharger is chosen as an example to demonstrate this optimisation method. Specifically, the influence of the pitch of the charging baffle on the particle–wall and particle–particle contact areas per particle per second is investigated. The design that maximises particle–wall contact area per particle per second and minimises particle–particle contact area per particle per second is considered an optimal one.

The pitch of the baffle is defined as the height of one 360°turn of the helix. Here, the height of the baffle is kept constant at 4.5 cm. The pitch angle is defined as the number of degrees through which the 4.5 cm baffle has been twisted (i.e., a pitch angle of 180°results in a pitch of 9 cm). Hence, decreasing the pitch angle loosens the helix, and increasing the pitch angle tightens it. Five different pitches were chosen for investigation, as shown in Fig. 5.

In all cases, the particle inlet velocity is assumed to be constant at 0.08 m/s under standard gravity. The inlet was positioned 1 cm above the top of the baffle to minimise overlap between bouncing particles and newly inserted particles.

3.3. Identifying an optimal design

An optimal baffle design will maximise the net particle–wall contact area per second spent transiting the charger, whilst minimising the net particle–particle contact area per second. Furthermore, an optimal

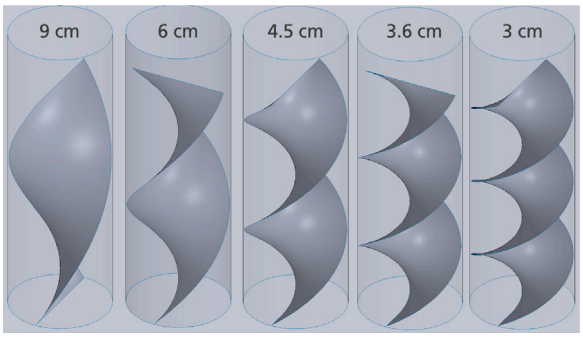

Fig. 5. CAD renderings of baffles designs with varying pitch (inset) evaluated in this study. The pitch angles are 180°, 270°, 360°, 450°, and 540°, respectively.

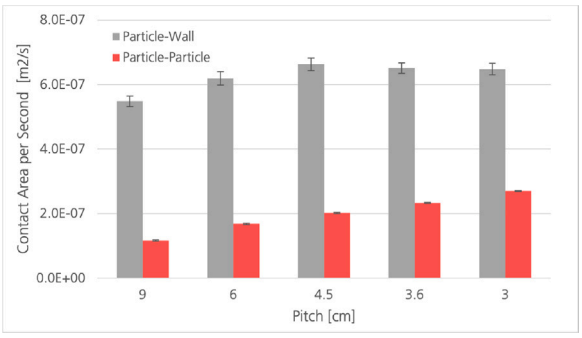

Fig. 6. Summary of the net particle–particle and particle–wall contact area accumulated per second for each charger design. Error bars indicate 95% confidence intervals.

design will maximise proportion of average particle–wall to particle–particle contact area, and will minimise the residence time of particles within the charger.

The aim of this work is to present a method to identify *an* optimal design using the DEM, rather than to find the optimal design for all cases. It is important to note that choice of particle and charger materials, particle size, charger geometries, and inlet flow rates may produce different optima. In this work, only one variable, baffle pitch, is modified to find an optimal arrangement. Furthermore, larger (>1 mm) particles were employed to avoid potential issues with adhesion to the charger walls during the experimental phase, as well as to minimise the computational cost of the simulations. This example of an optimised design may not necessarily be the optimal design for all of the materials studied.

To identify an optimum, each baffle design was tested using the DEM model with 150 PTFE particles with average radii of 3.18 mm. The net particle–particle and particle–wall contact areas were tracked separately, and the individual residence times within the charger were recorded.

A summary of the average particle–wall and particle–particle contact area accumulated per second of residence time are presented in Fig. 6. While there are statistically significant differences between the particle–particle contacts for all designs, the differences are less clear-cut for particle–wall contacts. The 9 cm design is a statistically significant minimum compared to the other designs. There is marginally significant maximum for the 4.5 cm pitch compared to the 6 cm pitch. However, there is no significant difference between the 6 cm, 3.6 cm, and 3 cm, nor between the 4.5 cm, 3.6 cm and 3 cm designs. This indicates that there is an effective break-even point at with at 6 cm design for particle–wall area. The ratio of particle–wall to particle–particle contact area for the 4.5 cm design is 11% lower than for the 6 cm design. Further, the 4.5 cm design represents a 32% increase in the average residence time per particle.

Taken together, the 6 cm design maximises the particle–wall contact area as well as the ratio of particle–wall to particle–particle contacts. It also offers appreciable increases in throughput compared to the 4.5 cm design. Hence, the 6 cm design is considered optimal in the context of this study. All subsequent simulations and experimental investigations have been performed using this design.

4. Experimental materials and methods

In this study, spherical polytetrafluoroethylene (PTFE), polyamide-66 (PA66) and polyvinylchloride (PVC) particles were used. To determine the DEM model parameters, the saturation charge and single-contact (particle–particle and particle–wall) charging behaviours were measured for each material. These tests were conducted with spherical particles with nominal radii of 3.18 mm and 4.76 mm procured from The Precision Plastic Ball Co. Ltd., of Addingham, England.

Subsequent tribocharging experiments using the optimised design were conducted with PTFE, PA66, and PVC. Three different particle radii were used for both PTFE and PA66 (0.794 mm, 1.59 mm, and 1.98 mm), whereas only 1.59 mm PVC particles were used. Again, all particles were procured from The Precision Plastic Ball Co. Ltd.

In all cases, the particles were washed in ethanol, dried, and neutralised using the Simco-Ion MEB bar prior to every experiment. The initial charge, q_0, of each particle (or sample) was measured by placing neutralised particles into a Faraday cup connected to a Keithley 6517b electrometer. All experiments, including the measurement of initial charges, were repeated at least 6 times.

Finally, all experiments were conducted under controlled environmental conditions using a sealed glove box. The temperature was maintained between 20-25 °C, and the relative humidity kept between 29%–33%.

4.1. Model parameter evaluation

An advantage of Rasera et al.'s [46] model parameters is that they can be evaluated using relatively common laboratory equipment. An aim of this study is to employ straightforward, easily-built experimental apparatuses to derive the model parameters. The outputs of the tribocharger models using these parameters are then evaluated against experimental data.

4.1.1. Saturation charge

The saturation charge of a given material is dependent upon the material that it is coming into contact with. For example, the saturation charge of a PTFE particle charged on aluminium will be different than that of the same particle charged on gold. For this study, the saturation charge of all three particle types and both particle sizes was found by manually shaking cleaned and neutralised single particles in containers made from PTFE, PA66, PVC, and aluminium. For tests involving insulating containers, the walls of the containers were neutralised using the Simco-Ion MEB bar prior to the introduction of the particle. The containers were shaken for 60 s, and then empties into the Faraday cup to measure the charge. Longer shaking times were investigated, however the saturation point was found to be unaffected. A summary of the saturation charge measurements is found in Table 1.

The theoretical surface saturation charge density for the 0.794 mm, 1.59 mm, and 1.98 mm particles are evaluated using Cruise et al.'s [7] method (Eq. (15)), and are summarised in Table 2.

Table 1
A summary of the saturation charge data for 3.18 mm and 4.76 mm PTFE, PVC and PA66 particles when charged against PTFE, PVC, PA66 and aluminium.

Cup material	Particle material	Rad. [mm]	$Q_{sat,avg}$ [C]	95% Conf. [C]
PTFE	PTFE	3.18	1.68×10^{-9}	1.35×10^{-10}
		4.76	3.23×10^{-9}	1.30×10^{-10}
	PVC	3.18	1.95×10^{-9}	7.84×10^{-11}
		4.76	3.38×10^{-9}	1.68×10^{-10}
	PA 66	3.18	2.28×10^{-9}	8.27×10^{-11}
		4.76	3.83×10^{-9}	1.48×10^{-10}
PVC	PTFE	3.18	-2.19×10^{-9}	7.48×10^{-11}
		4.76	-3.95×10^{-9}	2.04×10^{-10}
	PVC	3.18	1.50×10^{-9}	6.78×10^{-11}
		4.76	2.08×10^{-9}	2.29×10^{-10}
	PA 66	3.18	2.31×10^{-9}	7.87×10^{-11}
		4.76	4.39×10^{-9}	1.07×10^{-10}
PA 66	PTFE	3.18	-2.31×10^{-9}	6.64×10^{-11}
		4.76	-4.58×10^{-9}	2.17×10^{-10}
	PVC	3.18	-2.14×10^{-9}	9.94×10^{-11}
		4.76	-4.53×10^{-9}	1.59×10^{-9}
	PA 66	3.18	1.85×10^{-9}	7.81×10^{-9}
		4.76	3.21×10^{-9}	1.76×10^{-10}
Aluminium	PTFE	3.18	-1.51×10^{-9}	1.75×10^{-10}
		4.76	-2.94×10^{-9}	1.79×10^{-10}
	PVC	3.18	-1.43×10^{-9}	1.58×10^{-10}
		4.76	-2.82×10^{-9}	1.99×10^{-10}
	PA 66	3.18	3.15×10^{-10}	9.94×10^{-11}
		4.76	6.37×10^{-10}	2.25×10^{-10}

Table 2
Summary of the theoretical surface saturation charge densities for the 0.794 mm, 1.59 mm, and 1.98 mm particles used in the tribocharger DEM simulations and experimental verification studies. In general, smaller particles exhibit greater saturation surface charge density than larger particles of the same material [7].

Cup material	Particle material	Rad. [mm]	$\sigma_{sat,avg}$ [C/m^2]
PTFE	PTFE	0.794	3.08×10^{-5}
		1.59	1.91×10^{-5}
		1.98	1.68×10^{-5}
	PVC	1.59	-1.05×10^{-4}
	PA66	0.794	-3.03×10^{-4}
		1.59	-1.13×10^{-4}
		1.98	-7.52×10^{-5}
PVC	PTFE	0.794	-2.80×10^{-4}
		1.59	-1.05×10^{-4}
		1.98	-6.97×10^{-5}
	PVC	1.59	2.54×10^{-5}
	PA66	0.794	-3.07×10^{-4}
		1.59	-1.14×10^{-4}
		1.98	-7.50×10^{-5}
PA66	PTFE	0.794	3.25×10^{-4}
		1.59	1.20×10^{-4}
		1.98	7.94×10^{-5}
	PVC	1.59	1.21×10^{-4}
	PA66	0.794	4.51×10^{-5}
		1.59	2.48×10^{-5}
		1.98	2.07×10^{-5}
Aluminium	PTFE	0.794	-2.61×10^{-5}
		1.59	-1.66×10^{-5}
		1.98	-1.47×10^{-5}
	PVC	1.59	-1.53×10^{-5}
	PA66	0.794	4.76×10^{-6}
		1.59	3.25×10^{-6}
		1.98	2.94×10^{-6}

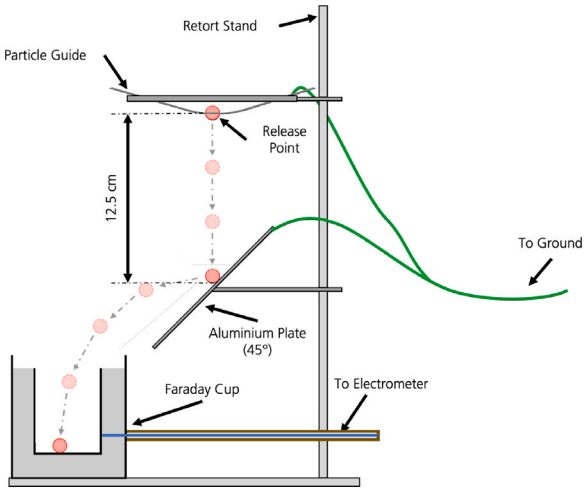

Fig. 7. A cartoon representation of the particle–wall single contact charge measurement apparatus.

4.1.2. Particle–wall single contact charging

The charge transfer due to single particle–wall interactions for both the 3.18 and 4.76 mm particles was measured by dropping neutralised particles from a fixed height (12.5 cm) onto a flat, aluminium plate angled at 45°. The dropped particles would hit the aluminium plate, and bounce into a Faraday cup to measure the charge. The apparatus used can be seen in Fig. 7. The design is based on that employed by Chowdhury et al. [71], with minor modifications to the particle support/release mechanism.

The particle support and release system consisted of two threaded rods bent into a shallow V-shape, supported by a retort stand ring and fixed in place using a putty-like adhesive. The rods were separated by slightly less than the radius of the particle being released. The neutralised particle was placed in the low-point of the dropping system. The supports were then gently separated using forceps. This approach allowed the particles to be dropped repeatedly from the same height, and did not impart any initial velocity. It should be noted that the initial charge was measured using the dropping system, and catching the particles in the Faraday cup. This was done to ensure that any charge imparted by the drop system was accounted for when calculating the model parameters.

The single contact particle–wall charge transfer data, along with the saturation surface charge densities, are used to evaluate the DEM particle–wall model parameters Γ (per Eq. (13)), and κ_c(per Eq. (16)).

4.1.3. Particle–particle single contact charging

A similar set-up was used to measure the charge transfer due to single particle–particle interactions. Instead of an angled plate, a replica of the dropping system, referred to as the 'lower support', was used. The apparatus can be seen in Fig. 8.

The larger (4.76 mm) impactor particles were placed in the dropping system, and the smaller (3.18 mm) target particles were held by the lower support. The impactor particle would be released, striking obliquely the target particle, and pushing it into the Faraday cup. The larger diameter of the impactors prevented them from following the targets into the Faraday cup, and compromising the measurement.

Once again, the single contact particle–particle charge transfer data and saturation surface charge density data are used to evaluate the DEM model parameters for particle–particle interactions. Γ is found with Eq. (14), and κ_c by Eqs. (17)–(19).

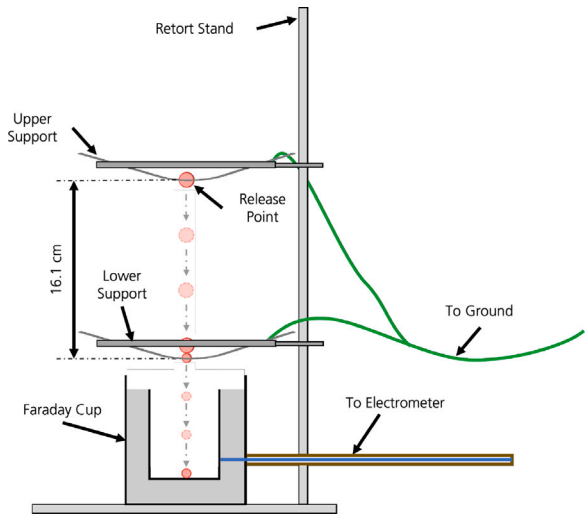

Fig. 8. A cartoon representation of the particle–particle single contact charge measurement apparatus.

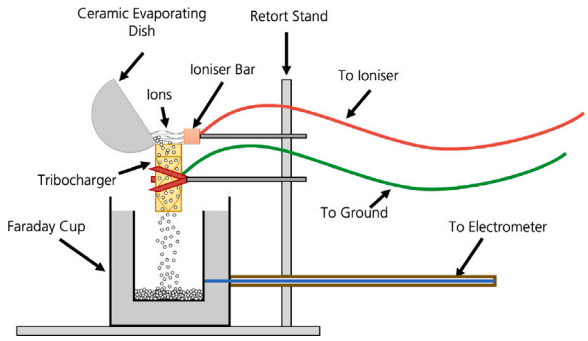

Fig. 9. A cartoon representation of the tribocharger charge measurement apparatus. Note that the same setup was used for the baseline measurements by replacing the charger with the baffle for an identical tube without the baffle.

4.1.4. Model parameter summary

The following tables summarise the model parameters evaluated from the experimental data. The contents of the tables are based off of the simulation cases being studied, as follows:

- Table 3 for single species, single size (SSSS) simulations
- Table 4 for single species, multi size (SSMS) simulations
- Table 5 for multi species, single size (MSSS) simulations
- Table 6 for multi species, multi size (MSMS) simulations

4.2. Tribocharger testing

Fifteen different particle samples were made to test the performance of the charger under different material conditions. A summary of the samples is found in Table 7.

It should be noted that the initial charge values employed in the simulations are based on the measured bulk charge of no-baffle condition from the SSSS cases. While this approach does not result in identical initial bulk charge values for the multi-species mixtures compared the experimentally-derived values, there is no way to determine the average particle charge of different species within a mixture without separating them by type prior to electrometer measurement. This is one likely source of error. For the SSMS cases, however, the experimental no-baffle charge values were used directly; the average particle charge was calculated as a function of net surface area per particle size.

Table 3
Summary of the key model parameters used in the single species, single size simulations. The minimum and maximum values for the model parameters were evaluated using the maximum and minimum experimental data values corresponding to 95% confidence intervals. For similar particles, Γ_{PP} is set to 0.

Particle material	r_{avg} [mm]	$Q_{i,avg}$ [C]		$\kappa_{c,PP}$	$\kappa_{c,PW}$	Γ_{PW}
PTFE	0.794	-4.72×10^{-13}	Min	2393.17	9.805	-1.79×10^{6}
			Avg	2462.50	14.265	-2.95×10^{6}
			Max	2552.11	19.656	-4.19×10^{6}
	1.59	-1.98×10^{-12}	Min	2665.37	9.805	-1.26×10^{6}
			Avg	2736.93	14.265	-1.88×10^{6}
			Max	2815.34	19.656	-2.51×10^{6}
	1.98	-4.54×10^{-12}	Min	2607.86	9.805	-1.15×10^{6}
			Avg	2757.38	14.265	-1.67×10^{6}
			Max	2929.97	19.656	-2.19×10^{6}
PVC	1.59	-9.16×10^{-13}	Min	6832.72	4.097	-1.30×10^{6}
			Avg	6981.02	8.541	-1.73×10^{6}
			Max	7142.00	13.962	-2.17×10^{6}
PA	0.794	1.38×10^{-13}	Min	3937.72	8.095	4.28×10^{5}
			Avg	4150.87	16.847	5.38×10^{5}
			Max	4433.33	34.686	6.47×10^{5}
	1.59	5.28×10^{-13}	Min	4914.77	8.095	2.71×10^{5}
			Avg	5052.73	16.847	3.67×10^{5}
			Max	5170.03	34.686	4.62×10^{5}
	1.98	8.75×10^{-13}	Min	5283.07	8.095	2.38×10^{5}
			Avg	5636.06	16.847	3.32×10^{5}
			Max	6051.37	34.686	4.26×10^{5}

The baffle of the tribocharger was build using a metal twisting jig. Aluminium strips were annealed, then bolted into the jig and twisted by 90°. After each twist, the strip was removed, and re-annealed to eliminate work hardening before twisting again. The tribocharger tube was cut from stock aluminium tubing with an inner diameter of 1.9 cm. The baffle was inserted into the tube and press-fit in place to avoid introducing other materials (glues, epoxies) that may interfere with the charging process.

The tribocharger testing apparatus supported the tribocharger using a flask clamp attached to a retort stand. The tribocharger was then suspended above the Faraday cup (Fig. 9). A separate flask clamp was used to support the Simco-Ion MEB neutralisation bar, oriented such that the ion source was aimed directly over the inlet of the tribocharger. This was done to ensure the particles were neutralised as best as possible prior to charging. An aluminium collar was added to the top of the tribocharger to prevent any bouncing particles from escaping. An identical aluminium tube without the optimised baffle insert was used to measure the 'zero' condition of the sample.

5. Results and discussion

In this section, the tribocharger DEM model performance is compared to experimental results. Further, an approach to predict approximately the charging behaviour of complex, heterogeneous mixtures from homogeneous SSSS simulation data is introduced.

5.1. Tribocharger performance modelling

To evaluate the performance of the tribocharger model, the four interaction regimes (SSSS, SSMS, MSSS, MSMS) were simulated using the parameters outlined in Tables 3 to 6. The simulation results were then compared to the experimental data collected for the same combinations particles. The bulk charge of the simulation outputs and experimental results are compared.

While bulk charge is both easily measured and indicative of the charging behaviour of the sample, it does not provide any insight to the charging behaviour of individual particles.

Table 4
Summary of the key model parameters used in the single species, multi size simulations. The minimum and maximum values for the model parameters were evaluated using the maximum and minimum experimental data values corresponding to 95% confidence intervals. For similar particles, Γ_{PP} is set to 0.

Material	$r_{avg,A}$ [mm]	$r_{avg,B}$ [mm]	$Q_{i,avg,A}$ [C]	$Q_{i,avg,A}$ [C]		κ_c (PP A-A)	κ_c (PP B-B)	κ_c (PP A-B)	Γ (PP A-B)	κ_c (PW A)	κ_c (PW B)	Γ (PW A)	Γ (PW B)
PTFE	1.98	0.794	-1.82×10^{-12}	-2.91×10^{-13}	Min	2607.86	2393.17	5.349	-4.78×10^{5}	9.805	9.805	-1.15×10^{6}	-1.79×10^{6}
					Avg	2757.38	2462.5	10.713	-1.58×10^{6}	14.265	14.265	-1.67×10^{6}	-2.95×10^{6}
					Max	2929.97	2552.11	21.652	-2.68×10^{6}	19.656	19.656	-2.19×10^{6}	-4.19×10^{6}
PA	1.98	0.794	1.06×10^{-12}	1.7×10^{-13}	Min	5283.07	3937.72	2.084	-2.51×10^{6}	8.095	8.095	2.38×10^{5}	4.28×10^{5}
					Avg	5636.06	4150.87	3.548	-2.76×10^{6}	16.847	16.847	3.32×10^{5}	5.38×10^{5}
					Max	6051.37	4433.33	5.093	-3.01×10^{6}	34.686	34.686	4.26×10^{5}	6.47×10^{5}

Table 5
Summary of the key model parameters used in the multi species, single size simulations. The minimum and maximum values for the model parameters were evaluated using the maximum and minimum experimental data values corresponding to 95% confidence intervals. For similar particles, Γ_{PP} is set to 0. In all cases, 1.59 mm particles were used.

Mat. A	Mat. B	Mat. C	$Q_{i,avg,A}$ [C]	$Q_{i,avg,B}$ [C]	$Q_{i,avg,C}$ [C]		$\kappa_{c,PP}$ (A-A)	$\kappa_{c,PP}$ (B-B)	$\kappa_{c,PP}$ (C-C)	$\kappa_{c,PP}$ (A-B)	$\kappa_{c,PP}$ (A-C)	Γ_{PP} (A-B)	$\kappa_{c,PP}$ (B-C)	Γ_{PP} (A-C)	Γ_{PP} (B-C)
PTFE	PA	–	-1.07×10^{-12}	2.67×10^{-13}	–	Min	2665.37	4914.77	–	1.865	–	-2.46×10^{7}	–	–	-
						Avg	2736.93	5052.73	–	2.611	–	-2.64×10^{7}	–	–	-
						Max	2815.34	5170.03	–	3.381	–	-2.82×10^{7}	–	–	-
PTFE	PVC	–	-1.03×10^{-12}	-9.28×10^{-13}	–	Min	2665.37	6832.72	–	2.01	–	-2.18×10^{7}	–	–	-
						Avg	2736.93	6981.02	–	3.23	–	-2.35×10^{7}	–	–	-
						Max	2815.34	7142	–	4.491	–	-2.53×10^{7}	–	–	-
PVC	PA	–	-2.24×10^{-13}	4.98×10^{-13}	–	Min	6832.72	4914.77	–	1.009	–	-2.47×10^{7}	–	–	-
						Avg	6981.02	5052.73	–	1.93	–	-2.65×10^{7}	–	–	-
						Max	7142	5170.03	–	2.897	–	-2.83×10^{7}	–	–	-
PTFE	PVC	PA	-1.05×10^{-12}	-9.47×10^{-13}	2.63×10^{-13}	Min	2665.37	6832.72	4914.77	2.01	1.865	9.805	1.009	4.097	8.095
						Avg	2736.93	6981.02	5052.73	3.23	2.611	14.265	1.93	8.541	16.847
						Max	2815.34	7142	5170.03	4.491	3.381	19.656	2.897	13.962	34.686

Mat. A	Mat. B	Mat. C	$\kappa_{c,PW}$ (A)	$\kappa_{c,PW}$ (B)	$\kappa_{c,PW}$ (C)	Γ_{PW} (A)	Γ_{PW} (B)	Γ_{PW} (C)
PTFE	PA	–	9.805	8.095	–	-1.26×10^{6}	2.71×10^{5}	–
			14.265	16.847	–	-1.88×10^{6}	3.67×10^{5}	–
			19.656	34.686	–	-2.51×10^{6}	4.62×10^{5}	–
PTFE	PVC	–	9.805	4.097	–	-1.26×10^{6}	-1.30×10^{6}	–
			14.265	8.541	–	-1.88×10^{6}	-1.73×10^{6}	–
			19.656	13.962	–	-2.51 $\times10^{6}$	-2.17×10^{6}	–
PVC	PA	–	4.097	8.095	–	-1.30×10^{6}	2.71×10^{5}	–
			8.541	16.847	–	-1.73×10^{6}	3.67×10^{5}	–
			13.962	34.686	–	-2.17×10^{6}	4.62×10^{5}	–
PTFE	PVC	PA	-2.18×10^{7}	-2.46×10^{7}	-2.47×10^{7}	-1.26×10^{6}	-1.30×10^{6}	2.71×10^{5}
			-2.35×10^{7}	-2.64×10^{7}	-2.65×10^{7}	-1.88×10^{6}	-1.73×10^{6}	3.67×10^{5}
			-2.53×10^{7}	-2.82×10^{7}	-2.83×10^{7}	-2.51×10^{6}	-2.17×10^{6}	4.62×10^{5}

Table 6
Summary of the key model parameters used in the multi species, multi size simulations. The minimum and maximum values for the model parameters were evaluated using the maximum and minimum experimental data values corresponding to 95% confidence intervals. For similar particles, Γ_{PP} is set to 0.

Mat. A	Mat. B	$r_{avg,A}$ [mm]	$r_{avg,B}$ [mm]	$Q_{i,avg,A}$ [C]	$Q_{i,avg,B}$ [C]		$\kappa_{c,PP}$ (A-A)	$\kappa_{c,PP}$ (BB)	$\kappa_{c,PP}$ (A-B)	Γ_{PP} (A-B)	$\kappa_{c,PW}$ (A)	$\kappa_{c,PW}$ (B)	Γ_{PW} (A)	Γ_{PW} (B)
PTFE	PA	1.98	0.794	-5.48×10^{-12}	5.45×10^{-13}	Min	2607.86	3937.72	1.865	-4.21×10^{7}	9.805	8.095	-1.15×10^{6}	4.28×10^{5}
						Avg	2757.38	4150.87	2.611	-4.52×10^{7}	14.265	16.847	-1.67×10^{6}	5.38×10^{5}
						Max	2929.97	4433.33	3.381	-4.84×10^{7}	19.656	34.686	-2.19×10^{6}	6.47×10^{5}
PTFE	PA	0.794	1.98	-2.29×10^{-13}	2.30×10^{-12}	Min	2393.17	5283.07	1.865	-4.05×10^{7}	9.805	8.095	-1.79×10^{6}	2.38×10^{5}
						Avg	2462.5	5636.06	2.611	-4.32×10^{7}	14.265	16.847	-2.95×10^{6}	3.32×10^{5}
						Max	2552.11	6051.37	3.381	-4.61×10^{7}	19.656	34.686	-4.19×10^{6}	4.26×10^{5}

5.1.1. Single species, single size

The first, and most straightforward, cases evaluated consists of particles of individual species and sizes. Three sizes of PTFE and PA66 are used. Only one size of PVC was used due to limited availability of particles from the supplier. A summary of the experimental and simulations results is found in Fig. 10.

In all but one case (0.794 mm PTFE), the experimental data falls within the predicted range of values from the simulations. The experimental data collected for each sample under both the zero (without baffle) condition and tribocharger (with baffle) condition (Table 8) demonstrates consistency. However, the change in surface charge density for the 0.794 mm sample is appreciably lower than for the two larger sizes (Fig. 11).

Analysis of the raw electrometer data reveals statistically significant differences in the particle feed rates between the 0.794 mm samples and both of the larger samples. The particle feed rate is found to be approximately 107±19 particles/s for the 0.794 mm fraction compared to 46±6 particles/s and 44±6 particles/s for the 1.59 mm and 1.98 mm samples, respectively. As discussed in Section 3, a larger number of particles within the tribocharger volume at any given time will suppress the charge transfer. It is therefore likely that the increased particle flow rate resulted in a lower measured bulk charge for PTFE.

Future studies should therefore look to improve the control of the particle feed rate.

Table 7
Summary of the particle samples tested using the optimised tribocharger design.

Class	Mat. A	Rad. A	Qty. A	Mat. B	Rad. B	Qty. B	Mat. C	Rad. C	Qty. C
Single species, Single size	PTFE	0.794	300	–	–	–	–	–	–
		1.59	300	–	–	–	–	–	–
		1.98	300	–	–	–	–	–	–
	PA66	0.794	300	–	–	–	–	–	–
		1.59	300	–	–	–	–	–	–
		1.98	300	–	–	–	–	–	–
	PVC	1.59	300	–	–	–	–	–	–
Single species, Multi size	PTFE	0.794	150	PTFE	1.98	150	–	–	–
	PA66	0.794	150	PA66	1.98	150	–	–	–
Multi species, Single size	PTFE	1.59	150	PA66	1.59	150	–	–	–
	PTFE	1.59	150	PVC	1.59	150	–	–	–
	PVC	1.59	150	PA66	1.59	150	–	–	–
	PTFE	1.59	100	PVC	1.59	100	PA66	1.59	100
Multi species, Multi size	PTFE	0.794	150	PA66	1.98	150	–	–	–
	PA66	0.794	150	PTFE	1.98	150	–	–	–

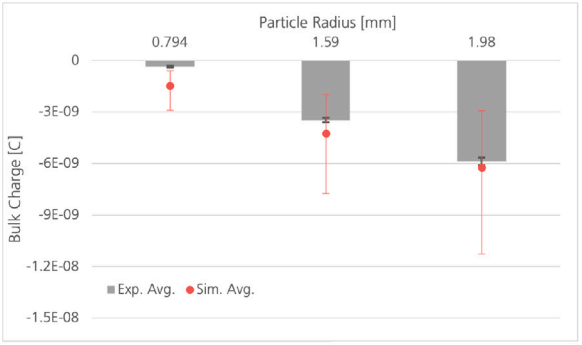

(a) PTFE particles.

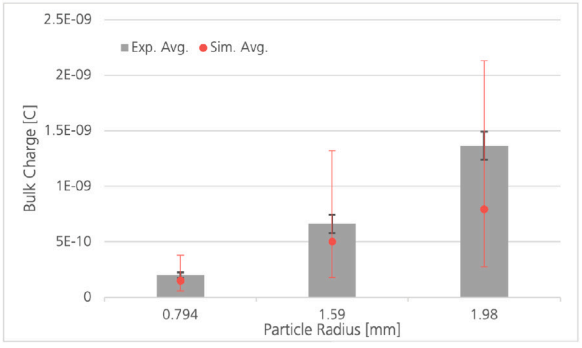

(b) PA66 particles.

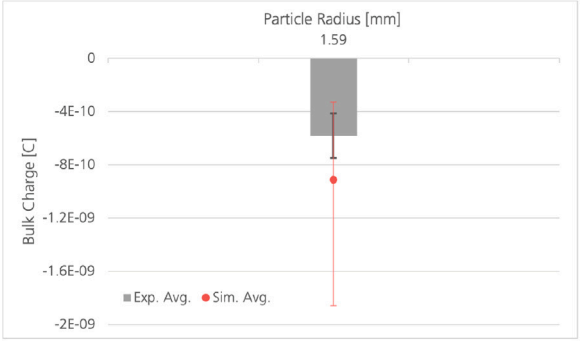

(c) PVC particles.

Fig. 10. Single species, single size simulation output versus experimental results for (a) PTFE, (b) PA66, and (c) PVC particles. Experimental error bars indicate 95% confidence intervals; simulation error bars indicate the range of outputs based on the maximum and minimum model parameter values summarised in Table 3.

Table 8
A summary of the experimental results for the zero (without baffle) condition and tribocharger (with baffle) condition for all sizes of PTFE particles. All confidence intervals are at least one order of magnitude lower than the average measurement. This indicates good consistency between experiments.

Radius [mm]	Without baffle [C] (95% Conf.)	With baffle [C] (95% Conf.)
0.794	-1.416×10^{-10} ($\pm 1.777 \times 10^{-11}$)	-4.989×10^{-10} ($\pm 3.118 \times 10^{-11}$)
1.59	-5.953×10^{-10} ($\pm 2.802 \times 10^{-11}$)	-4.064×10^{-9} ($\pm 1.045 \times 10^{-10}$)
1.98	-1.362×10^{-9} ($\pm 5.730 \times 10^{-11}$)	-7.232×10^{-9} ($\pm 1.607 \times 10^{-10}$)

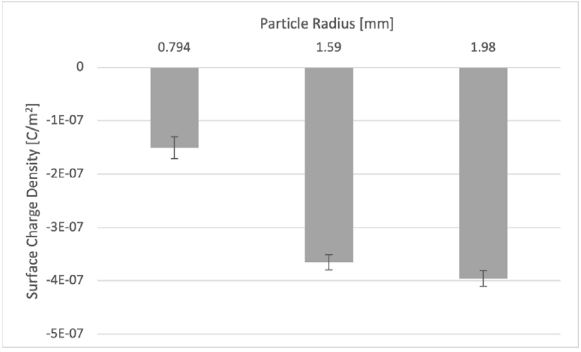

Fig. 11. Comparison of the change in surface charge density due to the tribocharger for each size fraction of PTFE. Error bars indicate 95% confidence intervals. In theory, all samples should experience similar changes in surface charge density, however the 0.794 mm sample attains appreciably less negative charge.

5.1.2. Single species, multi size

The output of the single species, multi size simulations and experiments are found in Fig. 12. While the model over-predicted the average bulk charge for the PTFE sample and under-predicted the average for the PA66 sample, there is good agreement with the range of maximum and minimum values.

5.1.3. Multi species, single size

For the four multi species, single size studies, there is generally good agreement with experimental results as seen in Fig. 13. The PVC-PA66 study, however, does not align with the experimental results. As mentioned previously, a mismatch of bulk charge does not necessarily imply that the charging behaviour of the sample is erroneous. Here, the simulation output is consistent with the bulk charging trends exhibited by the experimental data.

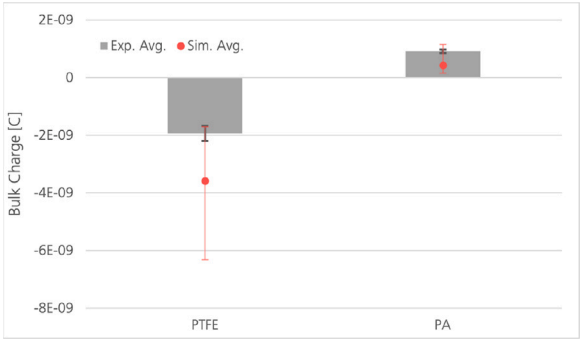

Fig. 12. Single species, multi size simulation output versus experimental results for PTFE and PA66 particles. Experimental error bars indicate 95% confidence intervals; simulation error bars indicate the range of outputs based on the maximum and minimum model parameter values summarised in Table 4.

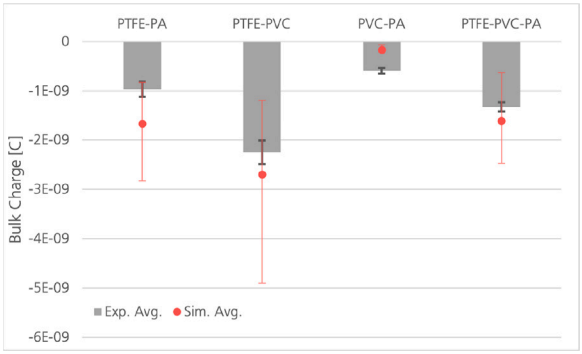

Fig. 13. Multi species, single size simulation output versus experimental results for PTFE/PA66, PTFE/PVC, PVC/PA66 and PTFE/PVC/PA66 mixtures. Experimental error bars indicate 95% confidence intervals; simulation error bars indicate the range of outputs based on the maximum and minimum model parameter values summarised in Table 5.

The differences between the model and experimental values for this case likely come down to the extrapolative approach used by Rasera et al. [46] to evaluate model parameters. This simulation may be improved by re-evaluating the model parameters using particles of the same size as those employed here.

5.1.4. Multi species, multi size

In the multi species, multi size case, the simulation outputs are dominated by the electronegativity of PTFE (Fig. 14). While this resulted in good agreement between the large PTFE/small PA66 simulation and experiments, there is no agreement with the small PTFE/large PA66 sample. Given, however, that the model tends to underestimate the average bulk charge of the single species, single size 1.98 mm PA66 sample, and overestimate the average for the 0.794 mm PTFE sample, it is not surprising that the model predicts a negative bulk charge for a mixture of these two species. The agreement between the model and experimental data could be improved through performing single-contact experiments using relevant particle sizes to evaluate the DEM model parameters, as mentioned in the previous section.

5.2. Predicting bulk charge from limited data

Minimising computational cost of simulations is always of interest in scientific computing. In this work, the average individual changes in particle charges determined by the single-species simulations are combined to predict the charging behaviour of mixtures. For example, assume a mixture consisting of 150 pieces of particle A with average $dQ_A = 1.0\ nC$ and 150 pieces of particle B with average $dQ_B = -2.0$

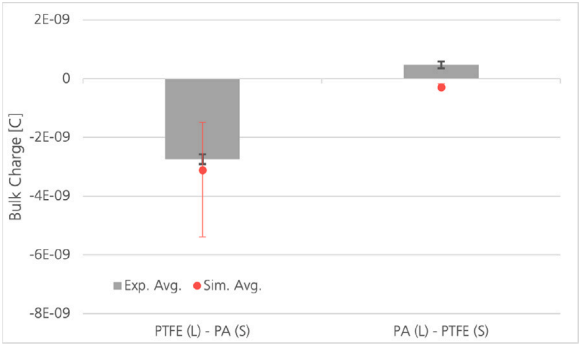

Fig. 14. Multi species, multi size simulation output versus experimental results for large PTFE/small PA66 and large PA66/small PTFE mixtures. Experimental error bars indicate 95% confidence intervals; simulation error bars indicate the range of outputs based on the maximum and minimum model parameter values summarised in Table 6.

nC. The predicted change in overall charge of the mixture would be: $150 \times (1.0 + (-2.0)) = -150$ nC.

This calculation is performed for all of the heterogeneous mixtures. The results are summarised in Table 9. The maximum and minimum values for the predicted range result from combining the maximum and minimum values of the individual species tests. In all cases, the range of predicted values intersect the experimental values. The overlap of predicted values and experimental data adds further support to the argument that the chosen design is optimal: had there been no overlap, it would indicate that stochastic particle–particle charging had greater impact on the charging behaviour. This is supported by the ratio of particle–particle to particle–wall contact areas in Table 9. It is worth noting that cases involving PTFE tend to perform better than those without and PTFE particles. This would support the notion that the design is an optimal one for PTFE, but not necessarily for other materials.

As a final test, the charging behaviour of a complex, five component mixture was predicted using the approach described above. The mixture consisted of 50 particles of each 0.794 mm PTFE, 0.794 mm PA66, 1.98 mm PTFE, and 1.98 mm PA66, along with 100 particles of 1.59 mm PVC. The mixture was then tested in the lab in the same manner as before. The results are observed in Fig. 15. There is excellent agreement between the predicted values and the experimental results. The experimental average and predicted average are within 5%, and the experimental confidence intervals fall within the range of maximum and minimum predicted values.

These results suggest that it is indeed possible to use limited data from single component simulations to predict, with good agreement, the bulk charging behaviour of complex mixtures. However, this approach should be considered as indicative only; it is not recommended as a substitute for more thorough modelling or experimental work. This is due to the wide range of potential predicted values from the linear combinations of maxima and minima.

6. Conclusions

In this work, a novel approach using the DEM to optimise the design of a tribocharger is detailed and demonstrated. A straightforward method for measuring single particle–particle and particle–wall contacts is described. The determination of the modelling parameters Γ and κ_c from the experimental data is presented. To validate the model parameters and charger design, 15 different particle samples were prepared and charged in the laboratory using the proposed design. Good agreement is found between the bulk sample charge and the predicted range output by the DEM model in 12 of the 15 cases.

Of the three cases that did not agree, the 0.794 mm single species PTFE case is explained by lack of control over the particle feed rate

Table 9
A comparison of the bulk charge predicted from combining single species, single size data with the full simulation outputs and the experimental data. The range for the simulation and prediction values come from the maximum and minimum model parameters outlined in Tables 3–6. The predicted ranges intersect the experimental averages in all cases. The ratio of particle–particle to particle–wall contact areas indicates that particle–wall contacts are dominant in all cases, though tends to be better for cases using PTFE.

	Simulation range [nC]	Predicted range [nC]	Experimental average (±95% CI) [nC]	Ratio of PP/PW (±95% CI)
SSMS				
PTFE	−1.70 : −6.32	−1.77 : −7.08	−1.93 (±2.61)	22.40% (±1.63%)
PA66	1.50 : 1.15	1.67 : 1.25	9.21 (±5.93)	29.81% (±3.03%)
MSSS				
PTFE/PA66	−8.25 : −2.83	−8.06 : −3.85	−9.17 (±1.21)	30.80% (±2.58%)
PTFE/PVC	−1.19 : −4.90	−1.16 : −4.81	−2.25 (±2.42)	33.47% (±2.45%)
PVC/PA66	−1.19 : −2.68	+4.96 : −8.39	−6.62 (±7.58)	45.75% (±4.59%)
PTFE/PVC/PA66	6.32 : −2.47	−3.32 : −3.14	−1.33 (±9.20)	33.16% (±3.04%)
MSMS				
L-PTFE/S-PA66	−1.45 : −5.40	−1.27 : −5.60	−2.74 (±1.65)	22.80% (±2.60%)
L-PA66/S-PTFE	−1.55 : −2.87	7.61 : −1.31	4.70 (±1.18)	19.34% (±1.22%)

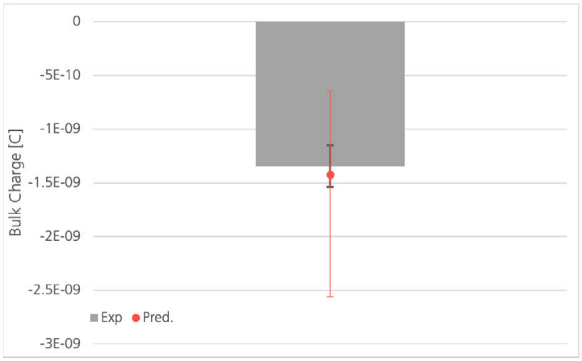

Fig. 15. Predicted bulk charge versus experimentally derived bulk charge for a 5-part, multi species, multi size mixture. Experimental error bars indicate 95% confidence intervals; prediction error bars indicate the range of outputs based on the maximum and minimum model parameter values summarised in Table 3.

in the experimental condition which resulted in lower than expected bulk charge measurements. The other two unaligned cases, single size mixture of PVC and PA66 and the multi species, multi size mixture of large PA66 and small PTFE, are likely explained by the extrapolative nature of Rasera et al.'s [46] model parameter determination method. Regardless, whilst the simulation outputs did not align well for these three cases, the overall charging trends relative to their respective cohorts were consistent with the experimental data. And, whilst bulk charge is a useful metric to evaluate the performance of the model with the experimental data, and to develop an understanding of the performance with different mixtures, it fails to capture the charge of individual particles, or even just particle types. The ultimate goal of a tribocharger is not to simply achieve a certain bulk charge; rather, the aim is to impart sufficient charge on particles to facilitate their separation. Subsequent evaluation of the performance of this optimised design, taking into account the impact of separation, is necessary.

Finally, this work presents a method for predicting the bulk charge of complex, multi-component mixtures from single-species simulation data. These predictions are found to intersect the experimental data in all cases. The bulk charge of a complex, five-part mixture was predicted using this approach, and very good agreement was found with the experimental data. This approach offers a good rule-of-thumb to predict potential bulk charging behaviour of different tribocharger designs from limited input data.

CRediT authorship contribution statement

J.N. Rasera: Conceptualisation, Computational Methodology, Investigation, Data analysis, Writing – original draft, Writing – review & editing. **J.J. Cilliers:** Supervision, Funding acquisition, Resources , Writing – review & editing. **J.-A. Lamamy:** Supervision, Industrial partner. **K. Hadler:** Supervision, Writing – review & editing.

Declaration of competing interest

The authors declare the following financial interests/personal relationships which may be considered as potential competing interests: J.N. Rasera reports financial support was provided by National Research Fund of Luxembourg. J.N. Rasera reports financial support was provided by Natural Sciences and Engineering Research Council of Canada. J.N. Rasera reports financial support was provided by ispace Europe S.A.J.N. Rasera reports equipment, drugs, or supplies was provided by Itasca Consulting Group, Inc.

Data availability

Data will be made available on request.

Acknowledgements

This research has been made possible through the support of the Luxembourg National Research Fund (FNR) under Industrial Fellowship Grant 12489764.

The authors acknowledge the support of the Natural Sciences and Engineering Research Council of Canada (NSERC) [ref: 411291661]. Cette recherche a été financée par le Conseil de recherches en sciences naturelles et en génie du Canada (CRSNG), [réf: 411291661].

The authors acknowledge the generous support of Itasca Consulting Group for the provision of a PFC license as well as support and mentorship from Dr D.O. Potyondy for J.N. Rasera through the Itasca Educational Partnership Program.

The authors would like to thank Mr S.O. Starr for his valuable feedback and insights.

References

[1] D.J. Lacks, The unpredictability of electrostatic charging, Angew. Chem. Int. Ed. 51 (28) (2012) 6822–6823.
[2] D.J. Lacks, A. Levandovsky, Effect of particle size distribution on the polarity of triboelectric charging in granular insulator systems, J. Electrost. 65 (2) (2007) 107–112.
[3] S.R. Waitukaitis, V. Lee, J.M. Pierson, S.L. Forman, H.M. Jaeger, Size-dependent same-material tribocharging in insulating grains, Phys. Rev. Lett. 112 (21) (2014) 218001.
[4] H. Zhao, G.P. Castle, I.I. Inculet, A.G. Bailey, Bipolar charging of poly-disperse polymer powders in fluidized beds, IEEE Trans. Ind. Appl. 39 (3) (2003) 612–618.
[5] S. Trigwell, N. Grable, C.U. Yurteri, R. Sharma, M.K. Mazumder, Effects of surface properties on the tribocharging characteristics of polymer powder as applied to industrial processes, IEEE Trans. Ind. Appl. 39 (1) (2003) 79–86.

[6] L. Xie, N. Bao, Y. Jiang, J. Zhou, Effect of humidity on contact electrification due to collision between spherical particles, AIP Adv. 6 (3) (2016) 035117.

[7] R.D. Cruise, K. Hadler, S.O. Starr, J.J. Cilliers, The effect of particle size and relative humidity on triboelectric charge saturation, J. Phys. D: Appl. Phys. (2022) http://dx.doi.org/10.1088/1361-6463/ac5081.

[8] S.D. Cezan, A.A. Nalbant, M. Buyuktemiz, Y. Dede, H.T. Baytekin, B. Baytekin, Control of triboelectric charges on common polymers by photoexcitation of organic dyes, Nature Commun. 10 (1) (2019) 1–8.

[9] R. Mukherjee, S. Sansare, V. Nagarajan, B. Chaudhuri, Discrete Element Modeling (DEM) based investigation of tribocharging in the pharmaceutical powders during hopper discharge, Int. J. Pharm. 596 (2021) 120284.

[10] K. Sayfidinov, S.D. Cezan, B. Baytekin, H.T. Baytekin, Minimizing friction, wear, and energy losses by eliminating contact charging, Sci. Adv. 4 (11) (2018) eaau3808.

[11] K.C. Pingali, S.V. Hammond, F.J. Muzzio, T. Shinbrot, Use of a static eliminator to improve powder flow, Int. J. Pharm. 369 (1–2) (2009) 2–4.

[12] A. Iuga, L. Calin, V. Neamtu, A. Mihalcioiu, L. Dascalescu, Tribocharging of plastics granulates in a fluidized bed device, J. Electrost. 63 (6–10) (2005) 937–942.

[13] A. Iuga, A. Samuila, R. Morar, M. Bilici, L. Dascalescu, Tribocharging techniques for the electrostatic separation of granular plastics from waste electric and electronic equipment, Particul. Sci. Technol. 34 (1) (2016) 45–54.

[14] A. Silveira, M. Cella, E. Tanabe, D. Bertuol, Application of tribo-electrostatic separation in the recycling of plastic wastes, Process Saf. Environ. Prot. 114 (2018) 219–228.

[15] M.E.-M. Zelmat, M. Rizouga, A. Tilmatine, K. Medles, M. Miloudi, L. Dascalescu, Experimental comparative study of different tribocharging devices for triboelectric separation of insulating particles, IEEE Trans. Ind. Appl. 49 (3) (2013) 1113–1118.

[16] A.M. Benhafssa, T. Zeghloul, S. Messal, L. Dascalescu, K. Medles, Factors that influence the efficiency of a propeller-type tribocharging device for granular plastics, IEEE Trans. Ind. Appl. 53 (2) (2016) 1446–1451.

[17] B. Rodrigues, C. Saron, Electrostatic separation of polymer waste by tribocharging system based on friction with PVC, Int. J. Environ. Sci. Technol. 19 (3) (2022) 1293–1300.

[18] J. Li, G. Wu, Z. Xu, Tribo-charging properties of waste plastic granules in process of tribo-electrostatic separation, Waste Manage. 35 (2015) 36–41.

[19] M. Bilici, L. Dascalescu, C. Dragan, O. Fati, A. Iuga, A. Samuila, Tribocharging and electrostatic separation of mixed granular solids in fluidized bed devices, IEEE Trans. Dielectr. Electr. Insul. 18 (5) (2011) 1476–1483.

[20] G. Buda, M. Bilici, A. Samuila, L. Dascalescu, Experimental study of the tribocharging process of plastic granular materials on a vibratory feeder device, IEEE Trans. Dielectr. Electr. Insul. 20 (5) (2013) 1489–1496.

[21] T. Shinbrot, T.S. Komatsu, Q. Zhao, Spontaneous tribocharging of similar materials, Europhys. Lett. 83 (2) (2008) 24004.

[22] T. Noshiro, M. Takeuchi, M. Asanae, M. Ochiai, Influence of toner composition on its tribocharging characteristics, J. Soc. Powder Technol. Japan 36 (9) (1999) 679–684.

[23] J. Anderson, et al., A comparison of experimental data and model predictions for tribocharging of two-component electrophotographic developers, J. Imaging Sci. Technol. 38 (4) (1994) 378–382.

[24] J. Anderson, The effect of additives on the tribocharging of electrophotographic toners, J. Electrost. 37 (3) (1996) 197–209.

[25] K. Takagi, G. Castle, M. Takeuchi, Tribocharging mechanism of mono-component irregular and spherical toners in an electrophotographic development system, Powder Technol. 135 (2003) 35–42.

[26] K. Law, I. Tarnawskyj, D. Salamida, T. Debies, Tribocharging mechanism in a model xerographic toner, in: International Congress on Advances in Nonimpact Printing Technologies, 1994, pp. 122–125.

[27] E. Kelly, D. Spottiswood, The theory of electrostatic separations: A review Part I. Fundamentals, Miner. Eng. 2 (1) (1989) 33–46.

[28] E. Kelly, D. Spottiwood, The theory of electrostatic separations: A review part II. Particle charging, Miner. Eng. 2 (2) (1989) 193–205.

[29] E. Kelly, D. Spottiswood, The theory of electrostatic separations: A review part III. The separation of particles, Miner. Eng. 2 (3) (1989) 337–349.

[30] H.-R. Manouchehri, K. Hanumantha Rao, K. Forssberg, Review of electrical separation methods - Part 1: Fundamental aspects, Min. Metall. Explor. 17 (1) (2000) 23–36.

[31] H.-R. Manouchehri, K. Hanumantha Rao, K. Forssberg, Review of electrical separation methods - Part 2: Practical considerations, Min. Metall. Explor. 17 (3) (2000) 139–166.

[32] I.I. Inculet, M.A. Bergougnou, S. Bauer, Electrostatic beneficiation apparatus for fluidized iron and other ores, IEEE Trans. Ind. Appl. (6) (1972) 744–748.

[33] P.M. Ireland, Triboelectrification of particulate flows on surfaces: Part I—Experiments, Powder Technol. 198 (2) (2010) 189–198.

[34] P.M. Ireland, Triboelectrification of particulate flows on surfaces: Part II—Mechanisms and models, Powder Technol. 198 (2) (2010) 199–210.

[35] P.M. Ireland, K. Nicholson, Analysis and comparison of particle tribochargers, Miner. Eng. 24 (8) (2011) 914–922.

[36] P.M. Ireland, Dynamic particle-surface tribocharging: The role of shape and contact mode, J. Electrost. 70 (6) (2012) 524–531.

[37] J. Rasera, J. Cilliers, J. Lamamy, K. Hadler, The beneficiation of lunar regolith for space resource utilisation: A review, Planet. Space Sci. 186 (2020) 104879.

[38] D.J. Lacks, R.M. Sankaran, Contact electrification of insulating materials, J. Phys. D: Appl. Phys. 44 (45) (2011) 453001.

[39] R. Ciccu, R. Peretti, A. Serci, M. Tamanini, A. Zucca, Experimental study on triboelectric charging of mineral particles, J. Electrost. 23 (1989) 157–168.

[40] R. Dwari, K.H. Rao, P. Somasundaran, Characterisation of particle tribo-charging and electron transfer with reference to electrostatic dry coal cleaning, Int. J. Miner. Process. 91 (3–4) (2009) 100–110.

[41] J. Captain, S. Trigwell, E. Arens, A. Biris, J. Captain, J. Quinn, C. Calle, Tribocharging lunar simulant in vacuum for electrostatic beneficiation, in: AIP Conference Proceedings, Vol. 880, AIP, 2007, pp. 951–956.

[42] S. Trigwell, J.G. Captain, E.E. Arens, J.W. Quinn, C.I. Calle, The use of tribocharging in the electrostatic beneficiation of lunar simulant, IEEE Trans. Ind. Appl. 45 (3) (2009) 1060–1067.

[43] S. Trigwell, J. Captain, K. Weis, J. Quinn, Electrostatic beneficiation of lunar regolith: Applications in in situ resource utilization, J. Aerosp. Eng. 26 (1) (2012) 30–36.

[44] M.D. Hogue, C.I. Calle, P.S. Weitzman, D.R. Curry, Calculating the trajectories of triboelectrically charged particles using Discrete Element Modeling (DEM), J. Electrost. 66 (1–2) (2008) 32–38.

[45] M.D. Hogue, C.I. Calle, D. Curry, P. Weitzman, Discrete element modeling (DEM) of triboelectrically charged particles: revised experiments, J. Electrost. 67 (4) (2009) 691–694.

[46] J. Rasera, R. Cruise, J. Cilliers, J.-A. Lamamy, K. Hadler, Modelling the tribocharging process in 2D and 3D, Powder Technol. (2022) 117607.

[47] H. Yu, L. Xie, et al., Numerical simulation of particle size effects on contact electrification in granular systems, J. Electrost. 90 (2017) 113–122.

[48] L. Xie, G. Li, N. Bao, J. Zhou, Contact electrification by collision of homogenous particles, J. Appl. Phys. 113 (18) (2013) 184908.

[49] W. Hu, L. Xie, X. Zheng, Simulation of the electrification of wind-blown sand, Eur. Phys. J. E 35 (3) (2012) 1–8.

[50] J.-C. Laurentie, P. Traoré, C. Dragan, L. Dascalescu, Numerical modeling of triboelectric charging of granular materials in vibrated beds, in: 2010 IEEE Industry Applications Society Annual Meeting, IEEE, 2010, pp. 1–6.

[51] J. Laurentie, P. Traoré, L. Dascalescu, Discrete element modeling of triboelectric charging of insulating materials in vibrated granular beds, J. Electrost. 71 (6) (2013) 951–957.

[52] J. Kolehmainen, A. Ozel, C.M. Boyce, S. Sundaresan, A hybrid approach to computing electrostatic forces in fluidized beds of charged particles, AIChE J. 62 (7) (2016) 2282–2295.

[53] J. Kolehmainen, A. Ozel, C.M. Boyce, S. Sundaresan, Triboelectric charging of monodisperse particles in fluidized beds, AIChE J. 63 (6) (2017) 1872–1891.

[54] J. Kolehmainen, P. Sippola, O. Raitanen, A. Ozel, C.M. Boyce, P. Saarenrinne, S. Sundaresan, Effect of humidity on triboelectric charging in a vertically vibrated granular bed: Experiments and modeling, Chem. Eng. Sci. 173 (2017) 363–373.

[55] F.S. Ali, M.A. Ali, G. Castle, I. Inculet, Charge exchange model of a disperse system of spherical powder particles, in: Conference Record of 1998 IEEE Industry Applications Conference. Thirty-Third IAS Annual Meeting (Cat. No. 98CH36242), Vol. 3, IEEE, 1998, pp. 1884–1891.

[56] C. Pei, C.-Y. Wu, D. England, S. Byard, H. Berchtold, M. Adams, DEM-CFD modeling of particle systems with long-range electrostatic interactions, AIChE J. 61 (6) (2015) 1792–1803.

[57] P. Sippola, J. Kolehmainen, A. Ozel, X. Liu, P. Saarenrinne, S. Sundaresan, Experimental and numerical study of wall layer development in a tribocharged fluidized bed, J. Fluid Mech. 849 (2018) 860–884.

[58] L. Konopka, J. Kosek, Discrete element modeling of electrostatic charging of polyethylene powder particles, J. Electrost. 87 (2017) 150–157.

[59] N. Duff, D.J. Lacks, Particle dynamics simulations of triboelectric charging in granular insulator systems, J. Electrost. 66 (1–2) (2008) 51–57.

[60] K.M. Forward, D.J. Lacks, R.M. Sankaran, Charge segregation depends on particle size in triboelectrically charged granular materials, Phys. Rev. Lett. 102 (2) (2009) 028001.

[61] P.A. Cundall, A computer model for simulating progressive, large-scale movement in blocky rock system, in: Proceedings of the International Symposium on Rock Mechanics, 1971, 1971.

[62] P.A. Cundall, O.D. Strack, A discrete numerical model for granular assemblies, Geotechnique 29 (1) (1979) 47–65.

[63] L. Schein, M. LaHa, D. Novotny, Theory of insulator charging, Phys. Lett. A 167 (1) (1992) 79–83.
[64] I. Itasca Consulting Group, PFC — Particle Flow Code, ver. 6.0, 2018.
[65] C. Holm, Simulation Methods in Physics 1, Vol. 2013, Institute for Computational Physics. University of Stuttgart, 2012.
[66] S. Naik, S. Sarkar, V. Gupta, B.C. Hancock, Y. Abramov, W. Yu, B. Chaudhuri, A combined experimental and numerical approach to explore tribocharging of pharmaceutical excipients in a hopper chute assembly, Int. J. Pharm. 491 (1–2) (2015) 58–68.
[67] S. Naik, S. Sarkar, B. Hancock, M. Rowland, Y. Abramov, W. Yu, B. Chaudhuri, An experimental and numerical modeling study of tribocharging in pharmaceutical granular mixtures, Powder Technol. 297 (2016) 211–219.
[68] S. Matsusaka, M. Ghadiri, H. Masuda, Electrification of an elastic sphere by repeated impacts on a metal plate, J. Phys. D: Appl. Phys. 33 (18) (2000) 2311.
[69] J. Kolehmainen, A. Ozel, S. Sundaresan, Eulerian modelling of gas–solid flows with triboelectric charging, J. Fluid Mech. 848 (2018) 340–369.
[70] J.W. Quinn, J.G. Captain, K. Weis, E. Santiago-Maldonado, S. Trigwell, Evaluation of tribocharged electrostatic beneficiation of lunar simulant in lunar gravity, J. Aerosp. Eng. 26 (1) (2012) 37–42.
[71] F. Chowdhury, A. Sowinski, M. Ray, A. Passalacqua, P. Mehrani, Charge generation and saturation on polymer particles due to single and repeated particle-metal contacts, J. Electrost. 91 (2018) 9–15.